

AC Response Across the Metal–Insulator Transition of YBCO Josephson Junctions Fabricated with a Helium-Ion Beam

Adhilsha Parachikunnumal,¹ Nirjhar Sarkar,¹ Aravind Rajeev Sreeja,¹ Sreekar Vattipalli,¹ Rochelle Qu,¹ Jay C. LeFebvre,¹ Roger K. Lake,¹ and Shane A. Cybart^{1, a)}

Department of Electrical and Computer Engineering, University of California Riverside

(Dated: 28 January 2026)

Using focused helium ion beam (FHIB) irradiation, we fabricated in-plane, high- T_c $\text{YBa}_2\text{Cu}_3\text{O}_{7-\delta}$ (YBCO) Josephson junctions. By varying the dose of the irradiation, we tune the junction barriers from metallic (SNS) to insulating (SIS) and investigate how this transition affects microwave-driven dynamics. As the barrier transitions from metallic to insulating, the oscillatory response of the Shapiro steps to the RF power changes dramatically. On either side of the metal-insulator transition, the devices exhibit clean integer Shapiro steps without half-integer features, demonstrating that the current–phase relation is dominated by the first harmonic and that the excess current is minimal. The current-voltage response is well-described by the resistively, capacitively shunted junction model assuming a single-harmonic current–phase relation. This behavior indicates well-controlled junction properties suitable for a wide range of superconducting electronics, including detectors, mixers, and high-density integrated circuits.

The AC Josephson effect provides a direct link between frequency and voltage, forming the foundation for primary voltage standards used worldwide by national metrology institutes.¹ These standards rely on the generation of precise, quantized voltages, known as Shapiro steps,² under microwave irradiation. Beyond metrology, the AC response of Josephson junctions is essential for a variety of superconducting RF and microwave devices, including filters,³ mixers,⁴ and detectors.⁵

In many high-transition temperature (T_c) Josephson junctions, particularly weak-link type devices, low impedance and strong Andreev reflections give rise to excess current,⁶ and higher harmonic components in the current–phase relation (CPR).^{7,8} These effects often manifest as half-integer Shapiro steps and non-ideal AC behavior. While numerous high- T_c junction designs have been studied,^{8–11} controlling and understanding the AC response across different barrier types remains a central area of research.^{12,13} Focused helium ion beam (FHIB) irradiation offers a powerful method to define Josephson junction barriers with nanometer-scale precision.¹⁴ By varying the ion dose, the barrier can be smoothly tuned from normal metal to insulator for comparison of different devices constructed from a single $\text{YBa}_2\text{Cu}_3\text{O}_{7-\delta}$ (YBCO) thin film.^{14–17} Ion irradiated junctions have demonstrated excellent stability,^{18,19} reproducibility,^{19,20} and scalability,^{21–23} and they have been applied to a wide range of superconducting circuits, including SQUIDs,^{17,24,25} digital high- T_c electronics,^{26,27} and quantum devices.^{28–30}

Previous studies have provided a foundational understanding of the AC response of FHIB junctions.^{12,13,31} Building on this important work, we extend the investigation to explore what happens as the barrier changes from metallic to insulating. By fabricating a series

of FHIB-defined junctions spanning the metal-insulator-transition, we systematically study how the Shapiro step structure and RF power dependence evolve. This approach provides insight into how barrier properties govern AC Josephson dynamics and aids the future development of high- T_c FHIB devices for microwave applications.

FHIB Josephson junctions for this work were fabricated from commercially grown YBCO films deposited on cerium oxide-buffered, *r*-plane, 50-mm sapphire wafers.³² The YBCO layer was 40-nm thick, and before breaking vacuum, a 200-nm gold (Au) layer was deposited *in-situ* to provide low-resistance contacts.

The design of the test samples is shown in Fig. 1. Wafers were diced into 5-mm \times 5-mm chips (Fig. 1 inset). Each chip was patterned using laser lithography, and both the gold and YBCO layers were etched together with a broad-beam argon ion mill to define 4- μm -wide bridges (Fig. 1). To form junctions, the YBCO under the gold was uncovered at the intended site for FHIB

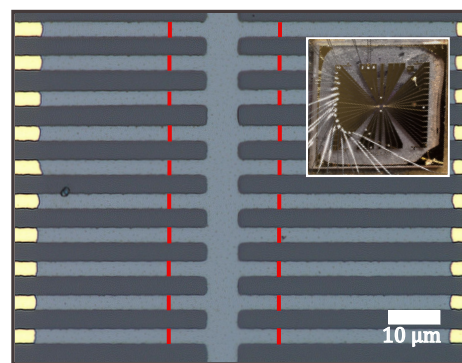


FIG. 1. Microscope image of a $100 \times 100 \mu\text{m}$ region showing twenty 4- μm -wide YBCO bridges where the Au layer was selectively removed to expose the underlying YBCO prior to focused helium-ion-beam irradiation of the junctions (red lines). The inset shows the full 5 \times 5 mm chip containing the four-point bridge structure.

^{a)}Electronic mail: cybart@ucr.edu

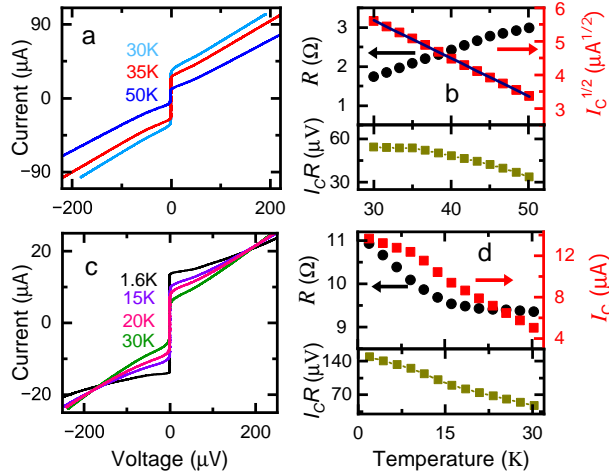


FIG. 2. Transport measurements of FHIB-fabricated Josephson junctions illustrating metallic and insulating barrier characteristics. (a) I – V characteristics of a SNS junction measured at 30, 35, and 50 K created with 2.0×10^{16} ions/cm². (b) $I_C^{1/2}$, R and their product vs temperature for the SNS junction. (c) I – V characteristics of a SIS junction measured at 1.6, 15, 20, and 30 K created with 3.0×10^{16} ions/cm². (d) I_C , R and their product vs temperature for the SIS junction.

irradiation. This was done using a second lithography step to selectively remove the gold in this area with a potassium iodide (KI^+) wet etch.

FHIB irradiation was performed at an accelerating voltage of 35 kV with a ~ 1 nm beam spot. The beam was scanned across the 4-μm-wide YBCO bridges to define narrow irradiated barriers; prior work established the barrier width to be < 3 nm.³³ Devices written at doses of 1.6 and 2.0×10^{16} ions/cm² exhibited superconductor–normal–superconductor (SNS) behavior, whereas devices written at 2.8, 3.0, and 3.4×10^{16} ions/cm² exhibited superconductor–insulator–superconductor (SIS) behavior. A device created with 2.4×10^{16} ions/cm² displayed intermediate (crossover) characteristics.

Four-point measurements were performed with the junctions cooled in a Quantum Design Dyna-Cool PPMS equipped with a μ -metal magnetic shield to reduce flux trapping. I – V characteristics were measured by current biasing the sample with a custom-built differential line driver; device signals were then amplified using SR560 battery-powered low-noise preamplifiers, and the amplified signals were recorded with a National Instruments data-acquisition system.

Figure 2 compares transport in a metallic-barrier (SNS) junction and an insulating-barrier (SIS) junction. Figures 2(a) and 2(c) show representative I – V curves at (30, 35, and 50 K) and (1.6, 15, 20, and 30 K) for the SNS and SIS junctions respectively. Additional temperatures were measured but omitted from the graph for clarity. Each I – V curve was fit with the resistively and capacitively shunted junction (RCSJ) model to extract the critical current (I_C) and resistance (R). The corresponding $I_C R$ product is shown below, which is plotted

versus temperature in Figs. 2(b) and 2(d) for all of the SNS and SIS devices, respectively.

For the SNS device, we plot ($I_C^{1/2}$) to highlight that the $I_C(T)$ follows a strongly coupled weak-link trend consistent with the de Gennes³⁴ description of SNS junctions, $I_C(T) = I_{C0} (1 - (T/T_c))^2$. The $R(T)$ in Fig. 2(b) decreases approximately linearly with decreasing temperature over the measured range, as typical for metallic YBCO.¹⁴ In contrast, the SIS device (Fig. 2(d)) shows $R(T)$ increasing as temperature decreases and $I_C(T)$ approaching a low-temperature plateau, consistent with YBCO SIS junctions.¹⁴ The distinct $I_C(T)$ and $R(T)$ trends across these two devices, together with intermediate-dose devices discussed below, demonstrate that focused helium-ion irradiation tunes the barrier continuously through the metal–insulator transition.

To investigate the AC Josephson response, microwave signals at 18 GHz were introduced to the junctions using a single conductor open coax cable for an antenna positioned next to the device inside the PPMS. The RF power was controlled by applying a 1 mHz ramp signal to the external amplitude modulation input of the waveform synthesizer. The devices were measured using the same four-point configuration described previously, with I – V characteristics shown in Fig. 2.

Figure 3 compares the microwave response of a representative SNS and SIS junction. Figures 3(a) and 3(b) show I – V characteristics measured with an 18 GHz RF signal (red) and without (black) for the SNS (30 K) and SIS (1.6 K) junctions respectively. In both junctions, we observe well-defined integer Shapiro steps and no half-integer steps or other parasitic features. In Figs. 3(c) and 3(d) we show the I – V characteristics at the same temperatures of the SNS and SIS junctions, respectively for different applied microwave powers. The curves are shifted vertically for clarity. The complete extinction of the step amplitudes is observed at each oscillation minimum, dropping cleanly to zero without any residual structure. These data provide a clear hallmark of high-quality Josephson behavior. The complete evolution of the RF response is shown in the differential resistance maps of Fig. (S1) in the Supplementary Materials (SM).

Figures 4(a) and 4(b) plot the measured step heights ($n = 0$ through $n = 4$) as a function of microwave source power for the SNS and SIS junctions respectively. The step heights follow the expected Bessel-like oscillations of the AC Josephson effect and are clearly resolved up to the fourth order.

The Kautz model provides a framework for rf-driven Josephson junctions operated in the low reduced-frequency regime $\Omega = f/f_c < 1$. Using this model, we compare our experimentally extracted Shapiro step currents with the predicted ideal values. For the SNS and SIS junctions, the measured $I_C R$ products are shown in Figs. 2(b) and 2(d), corresponding to characteristic frequencies $f_c \approx 26$ GHz and $f_c \approx 72$ GHz, respectively. At the measurement frequency $f = 18$ GHz, this yields $\Omega \approx 0.69$ (SNS) and $\Omega \approx 0.25$ (SIS). Using

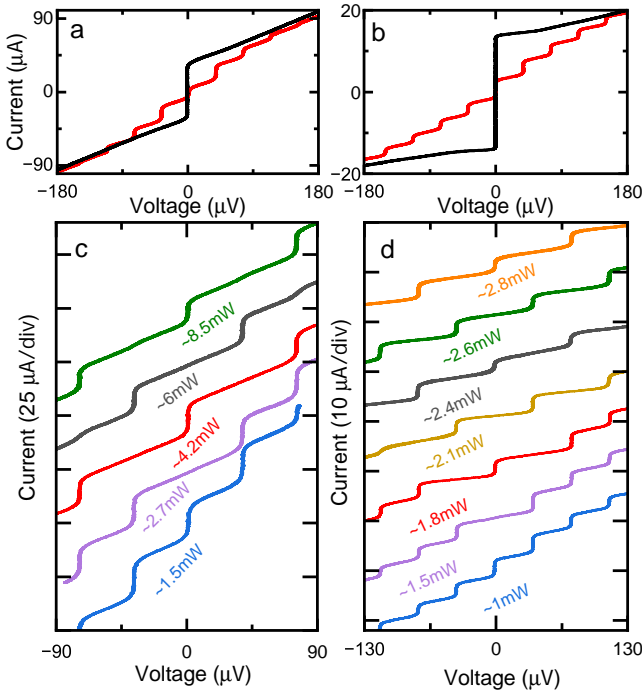


FIG. 3. I – V characteristics of an SNS (a) at 30 K and an SIS (b) at 1.6 K junctions, measured with 18 GHz irradiation (red), and without (black). (c) and (d) show the I – V characteristics of the same SNS (30 K) and SIS (1.6 K) junctions, respectively, for different applied microwave powers. These data illustrate that the step heights go to zero at the minima e.g. $n=1$ at 4.2 mW and 8.5 mW for the SNS junction.

a thin-film in-plane estimate for the Josephson penetration depth,³⁵ we obtain $\lambda_J \approx 5 \mu\text{m}$ for the SNS junction and $\lambda_J \approx 8.7 \mu\text{m}$ for the SIS junction. From Figs. 4(a) and 4(b), we extract the step heights of the $n = 1$ (ΔI_1) and $n = 2$ (ΔI_2) Shapiro steps and obtain simultaneous maximum step currents $\Delta I_{\max} \approx 12 \mu\text{A}$ for the SNS junction at $P_{\text{RF,SNS}} \approx 3.77 \text{ mW}$ and $\Delta I_{\max} \approx 2.4 \mu\text{A}$ for the SIS junction at $P_{\text{RF,SIS}} \approx 1.5 \text{ mW}$. Comparing these values to the Kautz point-contact prediction,³⁶ $\Delta I_{\max}^{\text{Kautz}} \approx 32.4 \mu\text{A}$ (SNS) and $5.8 \mu\text{A}$ (SIS), we obtain percentage differences of $\sim 62\%$ and $\sim 59\%$, respectively. Since the ion-irradiated junction length is on the 3-nm scale (short in the current-flow direction)³³ and the lateral width is comparable to λ_J , the junctions lie near the crossover between the point-contact and long junction limits. We therefore also compare our data to the corresponding long junction Kautz reference,³⁶ for which $\Delta I_{\max}^{\text{Kautz}} \approx 28.4 \mu\text{A}$ (SNS) and $\approx 2.8 \mu\text{A}$ (SIS), giving percentage differences of $\sim 58\%$ (SNS) and $\sim 14\%$ (SIS). Overall, these percentage differences likely reflect a combination of thermal noise in our measurements and the in-plane planar junction geometry, which falls between the ideal point-contact and strongly distributed limits; a dedicated model incorporating thin-film in-plane electrodynamics and rf coupling is therefore required for a fully quantitative description.

To analyze how the oscillation periodicity of the Shapiro step depends on source power, we fabricated an-

other device with doses of 1.6, 2.0, 2.4, 2.8, 3.0, and $3.4 \times 10^{16} \text{ ions/cm}^2$. Figure 5 displays the Shapiro step height as a function of source power for the zeroth-step oscillation in junctions spanning a wide range of resistances. SNS junctions fabricated with lower doses of 1.6 (Fig. 5(a)) and $2.0 \times 10^{16} \text{ ions/cm}^2$ (Fig. 5(b)) show resistances at 60 K of approximately 0.5Ω and 0.8Ω , and SIS junctions made with doses of 2.8 (Fig. 5(d)), 3.0 (Fig. 5(e)), and $3.4 \times 10^{16} \text{ ions/cm}^2$ (Fig. 5(f)) have resistances at 2 K of approximately 6Ω , 10Ω , and 12Ω , respectively. A crossover junction irradiated with $2.4 \times 10^{16} \text{ ions/cm}^2$ (Fig. 5(c)) has a resistance of $R \approx 2 \Omega$ at 30 K and occupies an intermediate regime in which the ion-irradiated region transitions from metallic to insulating character. This $2.4 \times 10^{16} \text{ ions/cm}^2$ device is the only junction that exhibits a clear crossover oscillation pattern: at low microwave power, it behaves like an SNS junction, showing the long-period oscillations characteristic of a metallic barrier, whereas at higher powers, as the junction is driven to larger voltages, the oscillations abruptly switch to the short-period behavior typical of an insulating (SIS) junction, as shown in the inset in Fig. 5(c). We have reproduced these behaviors across three chiplets with same ion irradiation; although the absolute resistance values vary slightly from chip to chip, the oscillation periodicity, the dose-dependent evolution, and in particular the $2.4 \times 10^{16} \text{ ions/cm}^2$ crossover signature are robust and reproducible.

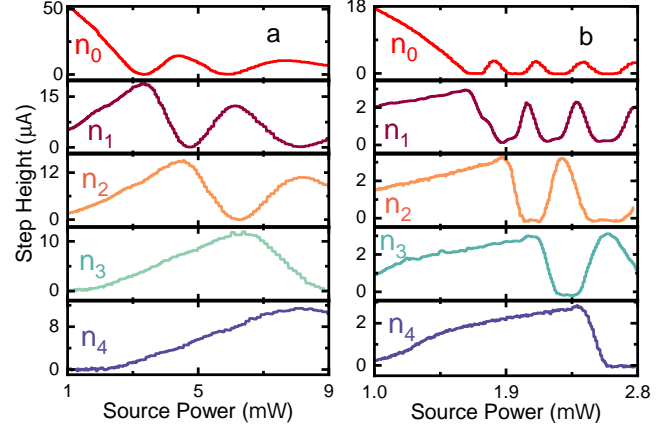


FIG. 4. Measured step heights of the zeroth through fourth order Shapiro steps as a function of applied microwave source power for the SNS junction (a) with $I_{\text{CR}} 54 \mu\text{V}$ at 30 K and the SIS junction (b) with $I_{\text{CR}} 150 \mu\text{V}$ at 1.6 K, showing Bessel-like oscillations.

To test for possible anharmonicity in the current–phase relation, we perform numerical simulations of the Shapiro step amplitudes as a function of the ac drive amplitude. Because the experiment is current biased and the main observable is the Shapiro step amplitude extracted from dc current–voltage characteristics under RF irradiation, we use a modified resistively and capacitively shunted junction (RCSJ)³⁷ model with thermal noise, which directly provides current–voltage curves for a current- bi-

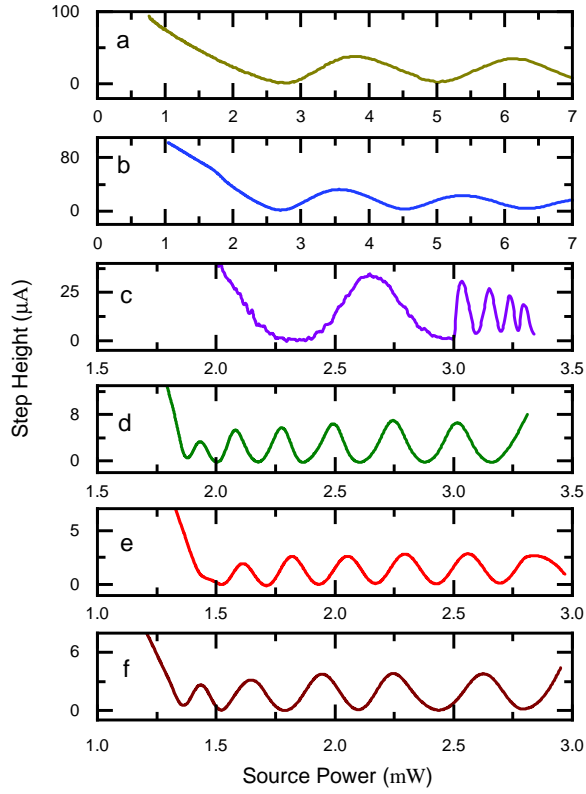


FIG. 5. Shapiro step height versus microwave source power for junctions on the same chip written with doses 1.6 (a) and, 2.0 (b) are measured at 60 K, 2.4 (c) at 30 K, and 2.8 (d), 3.0 (e), and 3.4×10^{16} ions/cm² (f) all measured at 2 K .

ased Josephson junction. The model details are described in the supplementary materials.

The junction parameters used in the simulations are chosen to match the experimental devices: for the SNS junctions we use $C = 10^{-16}$ F, $I_c = 170 \mu A$ and $R = 0.4 \Omega$, while for the SIS junctions³³ we use $C = 2.65 \times 10^{-15}$ F, $I_c = 70 \mu A$ and $R = 8.8 \Omega$. From the resulting I -V characteristics we extract the Shapiro step amplitudes as a function of i_{ac} , with particular attention to the zero-voltage ($n = 0$) step.

Figure 6 summarizes the comparison between experiment and the stochastic RCSJ model by showing the normalized zero-voltage ($n = 0$) Shapiro step amplitude \tilde{I} as a function of the ac drive. The blue squares represent the experimental data, and the solid curves are obtained from numerical solutions of Eq. (S2) in SM. Each theoretical curve consists of several hundred simulation points that are connected by lines as a guide to the eye. Because the RF signal experiences attenuation and impedance mismatch between the microwave line and the junction, the nominal source power does not coincide with the power actually delivered to the device. To place experiment and theory on a common scale, we assume that the RF power at the junction is given by the measured source power divided by a single constant factor for each device, which effectively accounts for these losses. This defines an effective RF power in the model, which we convert to an

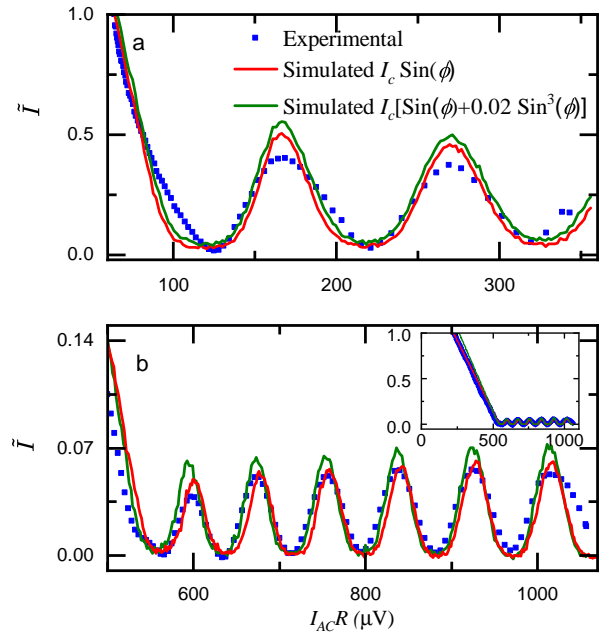


FIG. 6. Comparison of experimental data (blue scatter) and RCSJ model calculations for an SNS junction (a) from Figs 5(a) and an SIS junction (b) from Fig 5(e). Both datasets are fit using an ideal single-harmonic sinusoidal CPR (solid red lines) and a CPR with a third harmonic (dashed green lines). Experimental data are plotted (Fig. 5) versus source power rescaled by a constant factor, mapping the effective RF power $P \propto I_{AC}^2 R$ onto the effective voltage-drive $i_{ac} = I_{AC} R$ for direct comparison with theory. The vertical axis has been normalized to $\tilde{I} (I_{step}/I_{step,max} \text{ at lowest } I_{AC} R)$. The inset shows full range of the experimental and simulated data of SIS junction

ac current amplitude using $P \propto I_{AC}^2 R$ and then to the effective voltage-drive $I_{AC} R$. The constant factor is calculated to be 1.7×10^{-5} for the metallic junction and 2.9×10^{-5} for the insulator junction. The experimental points are therefore plotted as a function of source power rescaled by this constant factor, so that the horizontal axis can be compared directly with the theoretical dependence on i_{ac} and vertical axis has been normalized to $\tilde{I} (I_{step}/I_{step,max} \text{ at lowest } I_{AC} R)$.

In Fig. 6(a), the results for the SNS junction are displayed with two theoretical curves: one with a purely sinusoidal current-phase relation and one including a third-harmonic component with an amplitude equal to 2% of the first harmonic. The 2% value is obtained by minimizing the discrepancy between the calculated Shapiro step amplitudes and the experimental data in the oscillatory region of $\tilde{I}(i_{ac})$. Fits that attempted to include the low-amplitude, nearly linear regime tended to overfit that part of the data while underfitting the oscillatory behavior, so only the oscillatory region was used to evaluate the fitting error. Within this range, the third-harmonic term constitutes only a minor correction and does not appreciably improve the agreement compared with the purely sinusoidal model. This indicates

that the SNS current–phase relation can be treated, to good approximation, as single harmonic.

Figure 6(b) presents the corresponding analysis for the SIS junction, where a purely sinusoidal current–phase relation reproduces the measured step amplitudes over the full range of rescaled drive. Fig. 6(b) focuses on the high-drive region, while the inset shows the full drive range. For comparison, we also plot a curve with a 2% third-harmonic component, identical to that used for the SNS junction. This clearly deviates from the data and demonstrates that adding a third harmonic does not improve the fit. Overall, Fig. 6 shows that both SNS and SIS junctions are well described by an almost purely sinusoidal current–phase relation, with only a negligible ($\sim 2\%$) third-harmonic correction in the SNS case and no detectable higher-order term in the SIS junction. This observation is consistent with the clean integer Shapiro steps in Figs. 3 and (S1), confirming that both junctions display an almost ideal current phase relationship.

To account for the shorter apparent oscillation period of the SIS junction compared to the SNS junction in Fig. 5, we compare the datasets using the RF voltage scale $I_{AC}R$. When the data are expressed in terms of this junction-relevant drive parameter (Fig. 6), the apparent difference is strongly reduced and the oscillation periods become comparable. Quantitatively, the spacing between adjacent maxima is $\Delta V \approx 101 \mu\text{V}$ for the SNS junction and $\Delta V \approx 85 \mu\text{V}$ for the SIS junction. This trend is consistent with a voltage-source description of the RF coupling: in this picture, the Josephson current in the presence of an applied RF voltage is given by Eq. (S9), and the oscillation period is set by the ac voltage amplitude through the Bessel-function argument.

In summary, using focused helium ion beam irradiation, we fabricated high- T_c YBCO junctions that span the full range from metallic (SNS) to insulating (SIS) barriers. These devices exhibit clean integer Shapiro steps without half-integer features, demonstrating that the current–phase relation is dominated by the first harmonic and that excess current is minimal. This behavior indicates well-controlled junction properties suitable for a wide range of superconducting electronics, including detectors, mixers, and high-density integrated circuits.

ACKNOWLEDGMENTS

This work was supported by the Air Force Office of Scientific Research under Grants FA9550-20-1-144, FA9550-23-1-0369 and the Department of Energy NNSA grant DE-NA0004106.

- ¹C. A. Hamilton, *Review of Scientific Instruments* **71**, 3611 (2000).
- ²S. Shapiro, *Physical Review Letters* **11**, 80 (1963).
- ³M. Watanabe, P. D. Dresselhaus, and S. P. Benz, *IEEE Transactions on Applied Superconductivity* **16**, 49–53 (2006).
- ⁴J. Du, J. C. Macfarlane, C. M. Pegrum, T. Zhang, Y. Cai, and Y. J. Guo, *Journal of Applied Physics* **111**, 053910 (2012).
- ⁵V. V. Pavlovskiy, I. I. Gundareva, O. Y. Volkov, and Y. Y. Divin, *Applied Physics Letters* **116**, 082601 (2020).

- ⁶G. E. Blonder, M. Tinkham, and T. M. Klapwijk, *Physical Review B* **25**, 4515 (1982).
- ⁷D. B. Sullivan, R. L. Peterson, V. E. Kose, and J. E. Zimmerman, *Journal of Applied Physics* **41**, 4865 (1970).
- ⁸A. A. Golubov, M. Y. Kupriyanov, and E. Il'ichev, *Physical Review Letters* **81**, 894 (1998).
- ⁹H. Murakami, D. Akasako, M. Seto, *et al.*, *Czech Journal of Physics* **46**, 1345 (1996).
- ¹⁰J. Du, J. Lazar, S. Lam, E. Mitchell, and C. Foley, *Superconductor Science and Technology* **27**, 095005 (2014).
- ¹¹S. Cybart, K. Chen, and R. Dynes, *IEEE Trans. Appl. Supercon.* **15**, 241 (2005).
- ¹²F. Couédo, P. Amari, C. Feuillet-Palma, *et al.*, *Scientific Reports* **10**, 10256 (2020).
- ¹³Z. Chen, Y. Li, R. Zhu, J. Xu, T. Xu, D. Yin, X. Cai, Y. Wang, J. Lu, Y. Zhang, and P. Ma, *Chinese Physics Letters* **39**, 077402 (2022).
- ¹⁴S. A. Cybart, E. Cho, T. Wong, B. H. Wehlin, M. K. Ma, C. Huynh, and R. Dynes, *Nat. Nanotechnol.* **10**, 598 (2015).
- ¹⁵E. Y. Cho, Y. W. Zhou, J. Y. Cho, and S. A. Cybart, *Appl. Phys. Lett.* **113**, 022604 (2018).
- ¹⁶J. C. LeFebvre, A. Parachikunnumal, and S. A. Cybart, *Journal of Vacuum Science & Technology B* **42**, 063204 (2024).
- ¹⁷E. Y. Cho, M. K. Ma, C. Huynh, K. Pratt, D. N. Paulson, V. N. Glyantsev, R. C. Dynes, and S. A. Cybart, *Appl. Phys. Lett.* **106**, 252601 (2015).
- ¹⁸S. A. Cybart, P. Roediger, K. Chen, J. M. Parker, E. Y. Cho, T. J. Wong, and R. C. Dynes, *IEEE Transactions on Applied Superconductivity* **23**, 1100103 (2013).
- ¹⁹B. Müller, M. Karrer, F. Limberger, M. Becker, B. Schröppel, C. J. Burkhardt, R. Kleiner, E. Goldobin, and D. Koelle, *Physical Review Applied* **11**, 044082 (2019).
- ²⁰E. Cho, M. Ma, C. Huynh, K. Pratt, D. Paulson, V. Glyantsev, R. Dynes, and S. A. Cybart, *Appl. Phys. Lett.* **106**, 252601 (2015).
- ²¹J. C. LeFebvre and S. A. Cybart, *IEEE Transactions on Applied Superconductivity* **31**, 1 (2021).
- ²²S. A. Cybart, S. M. Anton, S. M. Wu, J. Clarke, and R. C. Dynes, *Nano Letters* **9**, 3535–3539 (2009).
- ²³J. C. LeFebvre, E. Y. Cho, H. Li, H. Cai, and S. A. Cybart, *Journal of Applied Physics* **131**, 163902 (2022).
- ²⁴E. Y. Cho, Y. W. Zhou, M. M. Khapaev, and S. A. Cybart, *IEEE Transactions on Applied Superconductivity* **29**, 1 (2019).
- ²⁵H. Li, H. Cai, N. Sarkar, J. C. LeFebvre, E. Y. Cho, and S. A. Cybart, *Applied Physics Letters* **124**, 192603 (2024).
- ²⁶H. Cai, J. C. LeFebvre, H. Li, E. Y. Cho, N. Yoshikawa, and S. A. Cybart, *Applied Physics Letters* **124**, 212601 (2024).
- ²⁷H. Cai, H. Li, E. Y. Cho, J. C. LeFebvre, and S. A. Cybart, *IEEE Transactions on Applied Superconductivity* **31**, 1 (2021).
- ²⁸Y.-J. Wu, M. Hack, K. Wurster, S. Koch, R. Kleiner, D. Koelle, J. Mannhart, and V. Harbola, *Applied Physics Letters* **125**, 032601 (2024).
- ²⁹C. Schmid, A. Jozani, R. Kleiner, D. Koelle, and E. Goldobin, *Physical Review Applied* **24**, 014041 (2025).
- ³⁰M. Pröpper, D. Hanisch, C. Schmid, M. Neumann, P. J. Ritter, M.-A. Tucholke, E. Goldobin, D. Koelle, R. Kleiner, M. Schilling, and B. Hampel, *IEEE Transactions on Applied Superconductivity* **35**, 1 (2025).
- ³¹A. T. Cortez, E. Y. Cho, H. Li, D. Cunnane, B. Karasik, and S. A. Cybart, *IEEE Transactions on Applied Superconductivity* **29**, 1 (2019).
- ³²Y.-T. Wang, R. Semerad, S. J. McCoy, H. Cai, J. LeFebvre, H. Grezdo, E. Y. Cho, H. Li, and S. A. Cybart, *IEEE Transactions on Applied Superconductivity* **29**, 1 (2019).
- ³³Y.-T. Wang, E. Y. Cho, H. Li, and S. A. Cybart, in *2019 IEEE International Superconductive Electronics Conference (ISEC)* (IEEE, 2019) pp. 1–3.
- ³⁴P. G. de Gennes, *Reviews of Modern Physics* **36**, 225 (1964).
- ³⁵S. K. Tolpygo and M. Gurvitch, *Applied Physics Letters* **69**, 3914 (1996).

³⁶R. L. Kautz, Journal of Applied Physics **78**, 5811 (1995).

³⁷D. McCumber, Journal of Applied Physics **39**, 3113 (1968).

AC Response Across the Metal–Insulator Transition of YBCO Josephson Junctions Fabricated with a Helium-Ion Beam

Adhilsha Parachikunnumal, Nirjhar Sarkar, Aravind Rajeev Sreeja, Sreekar Vattipalli, Rochelle Qu,
 Jay C. LeFebvre, Roger K. Lake, Shane A. Cybart (cybart@ucr.edu)
 Department of Electrical and Computer Engineering, University of California Riverside

SUPPLEMENTARY INFORMATION

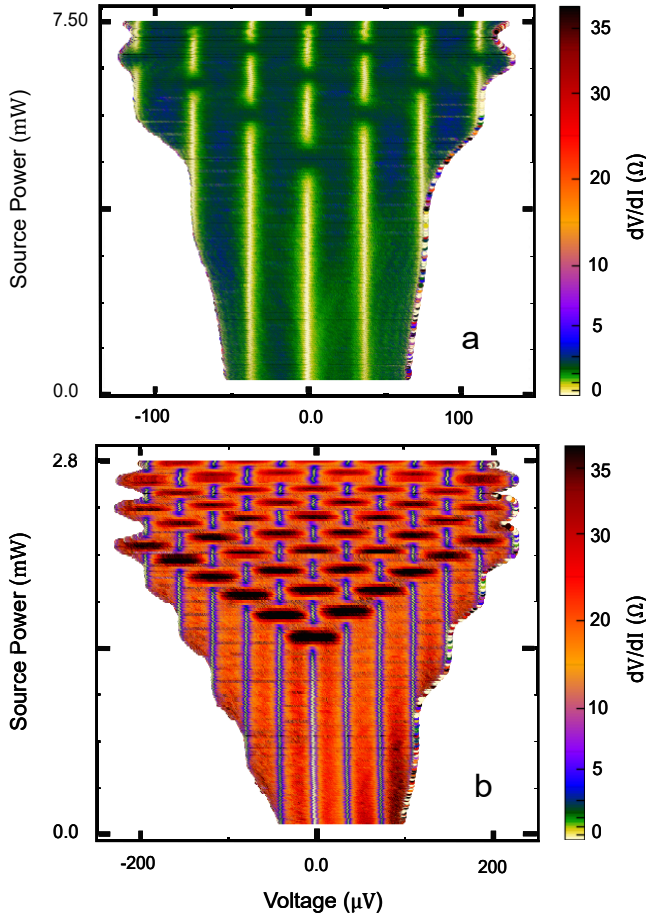


FIG. S1. Color maps of voltage vs microwave source power for (a) the SNS junction and (b) the SIS junction. These plots provide a detailed view of the microwave response, confirming the absence of half-integer steps and demonstrating the high quality of the junctions.

The complete evolution of the RF response is shown in the differential resistance maps of Fig. S1. These plots display dV/dI as a function of voltage and microwave power, revealing the Shapiro steps as sharp, uniform bands. The maps provide a compact visualization of the junction dynamics, confirming the absence of half-integer steps and other spurious resonances. This type of presentation highlights the clean, ideal AC Josephson behavior of both junction types and underscores the high quality of the FHIB-fabricated devices.

Resistively and Capacitively Shunted Junction (RCSJ) Model

In this description, the Josephson element is shunted by a resistance R and a capacitance C connected in parallel, so that dissipation and capacitive effects are treated consistently. The applied RF field in the experiment is represented in the simulations by an ac current term $I_{AC} \sin(\omega t)$ added to the dc bias I_{DC} , and a possible third-harmonic contribution to the current–phase relation is included through the modified RCSJ equation

$$I_{DC} + I_{AC} \sin(\omega t) = I_C [\sin \phi(t) + \alpha_3 \sin(3\phi(t))] + \frac{\Phi_0}{2\pi R} \dot{\phi}(t) + \frac{\Phi_0 C}{2\pi} \ddot{\phi}(t) + I_N(t), \quad (S1)$$

where $\phi(t)$ is the superconducting phase difference, I_{DC} and I_{AC} are the DC and AC bias currents, $I_N(t)$ represents thermal noise, Φ_0 is the flux quanta and α_3 is the anharmonicity parameter of the current–phase relation. The characteristic frequency and Stewart–McCumber parameter are defined as $\omega_c = 2\pi I_C R / \Phi_0$ and $\beta_C = 2\pi I_C R^2 C / \Phi_0$, respectively. Using the normalized time $\tau = \omega_c t$, the normalized currents $i_{dc} = I_{DC}/I_C$ and $i_{ac} = I_{AC}/I_C$, and the normalized drive frequency $\Omega = \omega/\omega_c$, Eq. (S1) can be written as

$$\beta_C \ddot{\phi} + \dot{\phi} + \sin(\phi(\tau)) + \alpha_3 \sin(3\phi(\tau)) = i_{dc} + i_{ac} \sin(\Omega\tau) + i_N(\tau), \quad (S2)$$

where dots now denote derivatives with respect to τ . Thermal fluctuations of the shunt resistor are modeled as Johnson–Nyquist noise with

$$\langle I_N(t_2) I_N(t_1) \rangle = \frac{2k_B T}{R} \delta(t_2 - t_1) \quad (S3)$$

which in normalized units, with $i_N(\tau) = I_N(t)/I_C$ and $\tau = \omega_c t$, yields the correlation

$$\langle i_N(\tau_2) i_N(\tau_1) \rangle = 2D \delta(\tau_2 - \tau_1) \quad (S4)$$

where D is a dimensionless noise strength.¹ Equations (S1)–(S4) thus provide a complete stochastic RCSJ description of the junction, which we use to compute the Shapiro step amplitudes as a function of the ac drive amplitude.

To obtain the Shapiro step amplitudes from the stochastic RCSJ model, we solve Eq. S2 numerically. The equation is integrated using the Euler–Maruyama scheme for stochastic differential equations, with Gaussian noise

consistent with the correlation in Eq. (S4). For computational efficiency, the algorithm is implemented in Fortran, which allows us to perform long time traces and fine sweeps of the control parameters. For each value of the normalized ac amplitude i_{ac} , we sweep the dc bias i_{dc} and integrate $\phi(\tau)$ over a long time interval. The normalized dc voltage is then obtained from the long-time average of the phase velocity,

$$\bar{v}(i_{\text{dc}}, i_{\text{ac}}) = \langle \dot{\phi}(\tau) \rangle_{\tau}, \quad (\text{S5})$$

which corresponds to the physical voltage $V = I_C R \bar{v}$.

Voltage-Source Model for an RF-Driven Josephson Junction

While our devices are current driven, the voltage-source model can be solved analytically and provides insight into the Shapiro step oscillation frequency. In this model, the Josephson device is driven by an ideal ac voltage source $V_s \cos \omega_s t$, so that

$$V(t) = V + V_s \cos \omega_s t. \quad (\text{S6})$$

Combining the ideal Josephson current relation $i_j(t) = I_c \sin \phi(t)$ with the second Josephson relation $d\phi/dt = (2e/\hbar)V(t)$ gives

$$i_j(t) = I_c \sin \left[\int_0^t \frac{2eV(t')}{\hbar} dt' + \phi_0 \right], \quad (\text{S7})$$

where ϕ_0 is a constant of integration. Substituting $V(t)$ and evaluating the integral yields

$$i_j(t) = I_c \sin \left[\omega_J t + \left(\frac{2eV_s}{\hbar\omega_s} \right) \sin \omega_s t + \phi_0 \right], \quad (\text{S8})$$

with the Josephson oscillation frequency defined as $\omega_J = 2eV/\hbar$. Expanding out the sine function in terms of Bessel functions gives

$$i_j(t) = I_c \sum_{n=-\infty}^{\infty} (-1)^n J_n \left(\frac{2eV_s}{\hbar\omega_s} \right) \sin[(\omega_J - n\omega_s)t + \phi_0], \quad (\text{S9})$$

Thus, the height of the Shapiro steps oscillate as a function of the applied ac voltage V_s , which scales as $I_{AC}R$.

¹G. Marchegiani, A. Braggio, and F. Giazotto, *Applied Physics Letters* **117**, 212601 (2020).